ACS APPLIED MATERIALS & INTERFACES

Forum Article

www.acsami.org

# Oxygen Vacancies Lead to Loss of Domain Order, Particle Fracture, and Rapid Capacity Fade in Lithium Manganospinel ($LiMn_2O_4$) Batteries

Xiaoguang Hao,[†] Xianke Lin,[‡] Wei Lu,[‡] and Bart M. Bartlett*[,†]

[†]Department of Chemistry, University of Michigan, 930 North University Avenue, Ann Arbor, Michigan 48109-1055, United States

[‡]Department of Mechanical Engineering, University of Michigan, 2350 Hayward Street, Ann Arbor, Michigan 48109, United States

Supporting Information

**ABSTRACT:** Spinel-structured lithium manganese oxide ($LiMn_2O_4$) has attracted much attention because of its high energy density, low cost, and environmental impact. In this article, structural analysis methods such as powder neutron diffraction (PND), X-ray diffraction (XRD), and high-resolution transmission and scanning electron microscopies (TEM & SEM) reveal the capacity fading mechanism of $LiMn_2O_4$ as it relates to the mechanical degradation of the material. Micro-fractures form after the first charge (to 4.45 V vs. $Li^{+/0}$) of a commercial lithium manganese oxide phase, best represented by the formula $LiMn_2O_{3.88}$. Diffraction methods show that the grain size decreases and multiple phases form after 850 electrochemical cycles at 0.2 *C* current. The microfractures are directly observed through microscopy studies as particle cracks propagate along the (1 1 1) planes, with clear lattice twisting observed along this direction. Long-term galvanostatic cycling results in increased charge-transfer resistance and capacity loss. Upon preparing samples with controlled oxygen contents, $LiMn_2O_{4.03}$ and $LiMn_2O_{3.87}$, the mechanical failure of the lithium manganese oxide can be correlated to the oxygen vacancies in the materials, providing guidance for better synthesis methods.

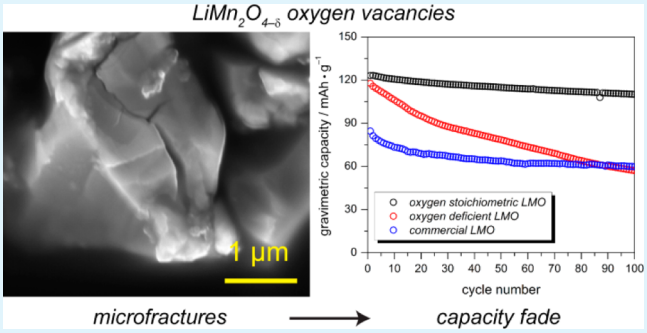


**KEYWORDS:** *neutron diffraction, point defects, Li-ion batteries, mechanical degradation, electron microscopy, energy storage*

## INTRODUCTION

Lithium-ion batteries have drawn much attention as energy storage devices for portable electronics, (hybrid) electric vehicles, and next-generation power grids because of their high volumetric and gravimetric energy densities.[1] The current research focus in lithium-ion batteries is developing high-voltage electrode materials with long-term reversible electrochemical stability. The rich lithium intercalation chemistry of transition metal oxides and polyanion complexes have enabled technological adoption of many candidates for cathode materials, such as $LiCoO_2$,[2] $LiNiO_2$,[3] $LiFePO_4$,[4] and the spinel-structured manganese oxides including $LiMn_2O_4$[5] and $LiNi_{0.5}Mn_{1.5}O_4$.[6] Carbon in the form of graphite[7] is the anode employed in current lithium-ion batteries.[8] However, the wide adoption of high-voltage cathodes is limited by electrode stability, with a particular focus on mitigating mechanical degradation.[9,10] Microfractures in cathodes composed of $LiCoO_2$[11,12] and $LiFePO_4$[13] powders have been observed in electron microscopy studies. Moreover, single-particle fracture during electrochemical cycling of $LiNiO_2$[14] is noticeable by optical microscopy. In addition, acoustic techniques have been employed to monitor fracture in $LiCoO_2$[15] and $MnO_2$[16] during cycling. Finally, atom probe tomography has also been applied to unveil the fracture mechanism of $LiCoO_2$ cathodes.[17,18] Mechanical fractures arise as stress builds during lithium insertion/extraction.[19,20] Although volume expansion is more pronounced at the anode materials because of the larger lattice changes,[21−25] cathodes have received less attention. In graphite, there is 12.8% volume expansion during charging. TEM experiments confirm the presence of cracks on the mesoscale during graphene layer exfoliation.[26] As a result, the internal resistance increases with a concomitant drastic capacity fade. On the basis of these experimental observations, theoretical calculations have been dedicated to simulate mechanical failure, which also provide insights into related capacity fading mechanisms.[27−30]

This manuscript is devoted to the cathode lithium manganese oxide, $LiMn_2O_4$ with a cubic symmetry spinel structure ($Fd\bar{3}m$) that delivers a considerable capacity of 148 mAh/g at 4.1 V (vs. $Li^{+/0}$). The electrochemical potential is derived from the $Mn^{3+/4+}$ formal redox couple. $LiMn_2O_4$ has

**Special Issue:** New Materials and Approaches for Electrochemical Storage

**Received:** February 2, 2014
**Accepted:** May 8, 2014
**Published:** May 20, 2014

  

the commercial advantage that is employs a low-cost metal that is nontoxic. However, the cyclability of $LiMn_2O_4$ is limited by oxygen vacancies in the crystal lattice, as we have previously reported.[31] Our work builds a connection between trace defects, structural changes, and electrochemical performance. In this study, we substantiate the capacity fading mechanism by conducting structural analysis to show that the electrochemical instability is tied to mechanical failure in $LiMn_2O_4$. Furthermore, based on our previous findings, we demonstrate that chemical composition can be controlled to minimize the capacity fade.

## EXPERIMENTAL SECTION

**General Considerations.** Lithium carbonate (99%), lithium metal foil (99.9%, metal basis) were purchased from Alfa Aesar. Manganese carbonate (99.9%, trace metal basis), lithium hexafluorophosphate (99.9%, battery grade), lithium hexafluoroarsenate (99%), lithium manganese oxide (electrochemical grade), and nitronium tetrafluoroborate (95%) were purchased from Sigma-Aldrich. *N*-Methyl-2-pyrrolidone (99%) and poly(vinylidene difluoride) (battery grade) were purchased from Alfa Aesar and used as received. Ethylene carbonate and diethyl carbonate were purchased from Sigma-Aldrich and were distilled prior to storing in an argon-filled glove box (Vacuum Atmospheres). HPLC-grade acetonitrile was purchased from Fisher and dried in a solvent purification system (Vacuum Atmospheres) then stored in a nitrogen-filled glove box (Vacuum Atmospheres). Extra dry oxygen gas was supplied by Cryogenic Gases.

Powder X-ray diffraction patterns were collected on a Bruker D8 Advanced diffractometer with a Lynx-Eye detector and parallel beam optics using Cu−K$\alpha$ radiation ($\lambda$ = 1.542 Å). The patterns were refined using the Bruker TOPAS software. Time-of-flight neutron diffraction experiments were performed on a powder diffractometer (POWGEN) at the Spallation Neutron Source of ORNL (Oak Ridge National Lab). The experimental resolution $\Delta d/d = 0.0015$ at $d$ = 1 Å. The data were collected at room temperature using incident neutron beam wavelengths centered at 1.066 and 3.198 Å. Scanning electron microscopy (SEM) images were collected using an FEI Nova Nanolab SEM/FIB. High resolution transmission electron microscopy (HR-TEM) was performed using a JEOL 3011 TEM with a $LaB_6$ electron beam source. The samples were dispersed in methanol and drop cast onto a copper grid with an ultrathin holey carbon film (Ted Pella). ICP-AES elemental analysis for lithium and manganese was obtained using a PerkinElmer Optima 2000DV analyzer. Typically, ∼10 mg samples were dissolved in 2−5 mL of 12 M HCl (Fisher Scientific) with a few drops of $H_2O_2$ (Fisher Scientific, 30 wt %) for quick digestion. The average oxidation states of manganese were determined by a potentiometric titration using $FeCl_2/KMnO_4$ (Alfa Aesar, 99.9% metal basis/98%). All samples were digested using dilute $H_2SO_4$ prior to titration. Differential scanning calorimetry was obtained with a DSC Q10 (TA Instruments) at a ramping rate of 10°C.

**Materials Preparation.** Commercial lithium manganese oxide (C-LMO) from Sigma-Aldrich was directly used as an active cathode material in this study. Chemical delithiation was performed by reacting lithium manganese oxide with nitronium tetrafluoroborate in acetonitrile. Typically, 1 gram of lithium manganese oxide reacted with 2 equiv of nitronium tetrafluoroborate. The reaction was kept under vigorous stirring for at least 96 h. The final products were collected by vacuum filtration and washed with fresh acetonitrile in the $N_2$ glove box.

Lithium manganese oxide samples with controlled oxygen content were also synthesized by a solid-state method. Lithium carbonate and manganese carbonate with the molar ratio 1.03 : 2 was ball-milled overnight. The extra 3% lithium content was used to compensate for potential lithium evaporation during the synthesis. Acetone was used for milling assistance. The acetone was then evaporated under reduced pressure with a rotary evaporator (Buchii). The carbonates were then calcined at 600 °C under pure oxygen flow (100 mL/min) with heating and cooling rates of 5°C/min. The product was then ground and annealed at 750 °C under oxygen, again with heating and cooling rates of 5°C/min. This sample was noted as S-LMO for synthesized LMO. The reaction yields on a ∼25 gram scale. To create oxygen vacancies in S-LMO, 5 grams of S-LMO was heated to 800 °C with a ramping rate of 10°C/min. After 30 min, the sample was removed from the furnace and directly quenched in liquid nitrogen. The sample noted as D-LMO for defect-LMO was then collected.

**Electrochemical Measurements.** Long-term electrochemical cycling tests were performed using coin cells or two-electrode Swagelok PTFE cells. For neutron diffraction sample preparation, the material was cycled in pouch cells. Pure lithium metal was used as the counter- and pseudoreference electrode for the measurements. To prepare the working electrode, we mixed Sigma-Aldrich lithium manganese oxide, carbon black (TIMCAL Super P), and poly-(vinylidene) difluoride (PVDF) (mass ratio of 85:10:5) in a Thinky AR-100 mixer. *N*-Methyl-2-pyrrolidone (NMP) was added to dissolve the PVDF binder. The composite was then cast onto a degreased aluminum foil by the doctor blade method. The foil was then dried in a vacuum oven (Fisher Scientific) at 120 °C overnight prior to assembling the electrochemical cells. The active material loading is approximately 11 mg/cm$^2$. The electrode masses were measured using a Sartorius ME36S microbalance. Celgard separator (model 3401) was used in the electrochemical tests. Lab-prepared electrolytes (1 M) were prepared using $LiPF_6$ and $LiAsF_6$ with ethylene carbonate and diethyl carbonate with volume ratio of 2:1. Commercial electrolyte of 1 M $LiPF_6$ in ethylene carbonate, dimethyl carbonate, and diethyl carbonate (v/v/v, 1:1:1) was also used as control from MTI. All cells were assembled in the argon glove box.

Galvonostatic charge/discharge experiments were performed on a NEWARE BTS-5 V1MA or a Maccor 64-channel cycler in the voltage window 3.40 to 4.45 V (vs. $Li^{+/0}$). The constant current applied in the charge/discharge test is 0.2 $C$ (where $C$ is the current required to discharge the theoretical capacity of the cell in 1 h). Cyclic voltammetry (CV) was recorded on a CH Instruments 660 C electrochemical workstation. Electrochemical impedance spectra (EIS) were collected on an Autolab PGSTAT302N with a FRA module. Prior to EIS measurements, the cells were equilibrated at 3.40 V until the current dropped below 10 nA. The AC perturbation was ±10 mV, and the frequency range was from $1 \times 10^5$ to $1 \times 10^{-2}$ Hz.

Electrochemical delithitation was applied for neutron sample preparation. The electrochemical cells were charged to the desired potential at 0.2 $C$ current; then the cell potential was held until the current dropped below 1 $\mu$A. The cell was then disassembled, and the cathode was washed with diethyl carbonate solvent and kept under a vacuum at room temperature. The active material was then carefully removed from the aluminum current collector by a razor blade. A similar treatment was used to collect the cathode material after 100 galvanostatic cycles at 0.2 $C$ current for the neutron diffraction study.

## RESULTS

Lithium manganese oxide ($LiMn_2O_4$) has a cubic spinel structure with a space group of $Fd\bar{3}m$ and a unique lattice parameter, $a$; in this structure, lithium, manganese and oxygen reside on the 8$a$ (tetrahedral), 16$d$ (octahedral), and 32$e$ Wyckoff sites, respectively. Conventional solid-state synthesis requires high-temperature annealing to form products with suitable crystallinity. However, oxygen vacancies can be easily introduced during the calcination reaction. In a previous study,[31] we used neutron diffraction to quantify the oxygen defects in hydrothermally synthesized $Li_{1+x}Mn_{2-x}O_{4-\delta}$, in which $\delta$ is the vacancy factor. In the present study, commercial $LiMn_2O_4$ (C-LMO) from Sigma-Aldrich was used because of its wide availability. The scanning electron microscopy (SEM) image in Figure 1a shows that particles range from 2−10 $\mu$m in size. Figure 1b shows the X-ray diffraction pattern of C-LMO with the corresponding Rietveld refinement (see Tables S1 and S2 in the Supporting Information). On the basis of the XRD

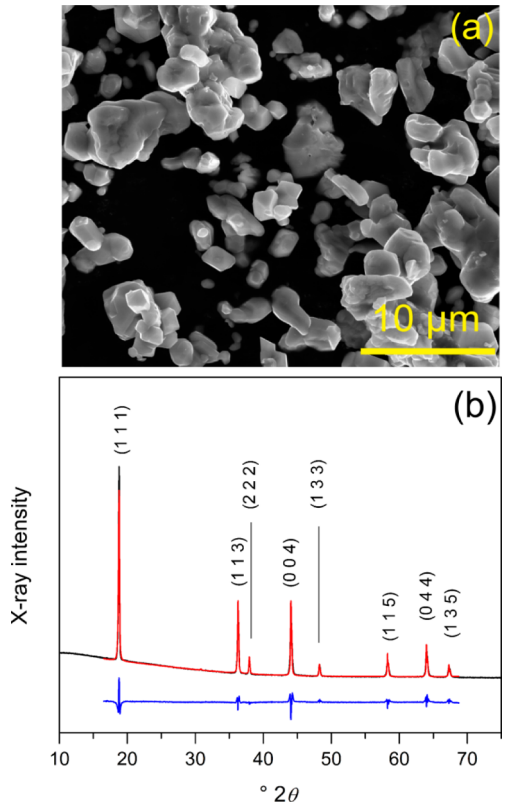


**Figure 1.** (a) SEM image of fresh C-LMO; (b) powder X-ray diffraction pattern (black), Rietveld refinement (red), and difference pattern (blue) for C-LMO.

result, C-LMO shows very high crystallinity without any detectable impurities. The structural refinement result gives a lattice parameter $a$ = 8.254 Å. The lattice parameter of stoichiometric $LiMn_2O_4$ is 8.248 Å.[32] We note that although the observed value is close to the literature value, the compound may be oxygen deficient.

Cyclic voltammetry (CV) and differential scanning calorimetry (DSC) indirectly provide evidence for oxygen vacancies in $LiMn_2O_4$. Figure S1a in the Supporting Information shows the CV trace collected at 0.1 mV/s of C-LMO. The redox waves centered about 4.0 V are indicative of lithium insertion and extraction chemistry. However, we also observe electrochemical reactions at ∼3.2 and 4.5 V, which are attributed to a phase change from a cubic cell to a double hexagonal cell that arises due to oxygen deficiency.[33] In addition, Figure S1b in the Supporting Information shows the DSC profile recorded during the cooling process. The exotherm at ∼10 °C suggests a phase change, which has also been shown to occur due to oxygen vacancies.[34,35] Finally, elemental analysis (see Table S3 in the Supporting Information) by ICP-AES analysis and potentiometric titration shows that C-LMO is best represented as the formula $LiMn_2O_{3.88}$, which confirms the oxygen non-stoichiometry in the material.

Figure 2 shows the neutron diffraction pattern of the fresh, uncycled C-LMO. As we expected, the site occupancies determined in the Rietveld refinement (see Table S4 in the Supporting Information) show evidence of oxygen deficiencies, and the formula unit is best represented as $LiMn_2O_{3.88}$. This formula is in excellent agreement with the elemental analysis. The oxygen atoms located on the 32*e* Wyckoff sites are calculated to be 97.1% filled, which confirms the oxygen

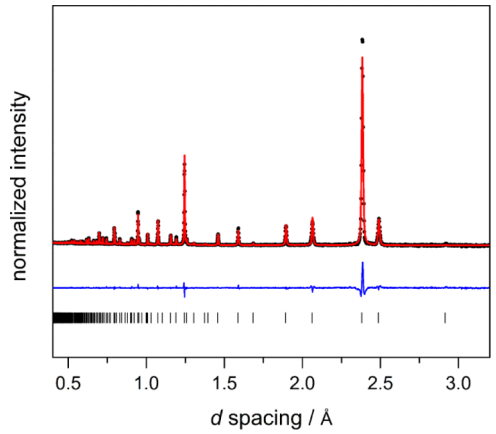


**Figure 2.** Neutron diffraction pattern obtained on POWGEN at 300 K of C-LMO; black dots represent the observed intensities, the red line is the fit, the blue line is the difference pattern, and the tick marks below the profiles indicate positions of all allowed Bragg reflections.

deficient structures of C-LMO. Meanwhile, the lattice parameter is 8.2530 Å, which corroborates the powder X-ray study.

We next carried out charge/discharge tests of a C-LMO battery between 3.40 to 4.45 V *vs.* $Li^{+/0}$ (lithium foil) in a lab-prepared electrolyte containing 1 M $LiPF_6$ in the typical carbonate solvents. To achieve detailed electrochemical behavior and to minimize energy losses due to polarization, a slow cycling rate of 0.2 *C* was used for all of the galvanostatic charge/discharge experiments in this work. The first charge/discharge cycling profile of C-LMO is plotted in Figure 3a. A sloping region and a pseudo-plateau are observed in both charging and discharging curves, corresponding to the single phase and two phase insertion/extraction, respectively. During the charging process of C-LMO, ∼120 mAh/g is stored, which corresponds to 81% of the theoretical capacity of $LiMn_2O_4$. However, only 84.5 mAh/g can be extracted during the first discharge process. That is, there is an ∼30% irreversible capacity loss during the first electrochemical cycle.

There are at least two reasons that explain this observation: active material loss due to acid corrosion and side reactions between C-LMO and the electrolyte that blocks lithium channels. For the first possibility, it is well-documented that trace moisture in the cell leads to HF formation from $LiPF_6$.[36] To test this possible degradation mechanism, we repeated the cycling experiment using the more hydrolytically stable $LiAsF_6$ electrolyte. Meanwhile, we also cycled the C-LMO cathode in a half-cell configuration at elevated temperature (55 °C) to study electrolyte degradation and capacity loss during the first cycle, noting that detrimental HF formation should be faster at higher temperature. Figure 3b shows the first charge/discharge profiles of C-LMO cycled under these different conditions. From this data, we conclude that the capacity fade is the same regardless of temperature and electrolyte formulation, and is an inherent property of C-LMO cathode material.

The 3.40−4.45 V electrochemical window does not include the irreversible phase transitions that occur at potentials <3.2 and >4.5 V. To determine whether detrimental changes occur at higher potential or if they occur throughout the entire electrochemical window, we collected the cathode material at a state-of-charge of 4.45 V to investigate possible microstructural variation after the first delithiation. The SEM image in Figure 4a shows unequivocal particle microfracture after the first


dx.doi.org/10.1021/am500671e | *ACS Appl. Mater. Interfaces* 2014, 6, 10849−10857

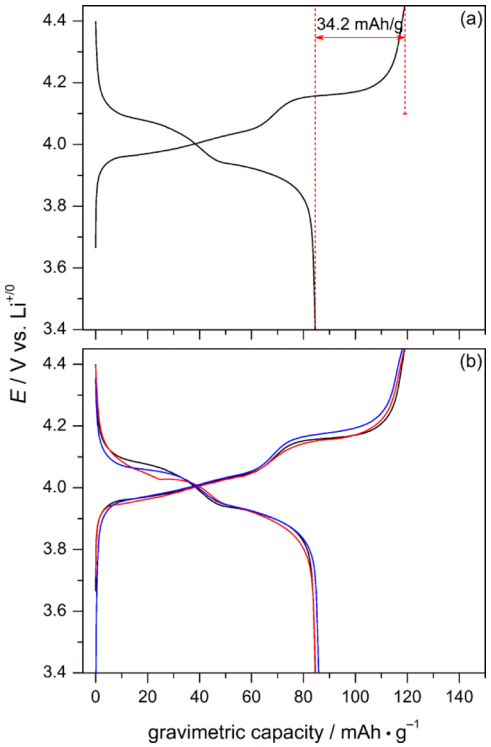


**Figure 3.** (a) First electrochemical charge/discharge cycle of C-LMO collected at 0.2 *C* current within the potential window of 3.40−4.45 V; (b) first electrochemical charge/discharge cycle of C-LMO collected at 0.2 *C* current within potential window of 3.40−4.45 V in different solvents: black, 1 M $LiPF_6$ in EC:DEC mixture with v/v of 2:1 at room temperature; red, 1 M $LiPF_6$ in EC:DEC mixture with v/v of 2:1 at 55°C; blue, 1 M $LiAsF_6$ in EC:DEC mixture with v/v of 2:1 at room temperature.

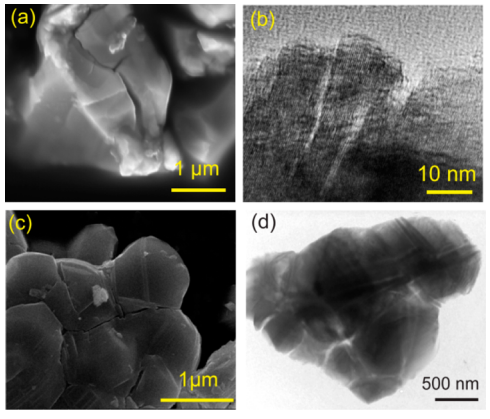


**Figure 4.** (a) SEM image of C-LMO after first charge at SOC of 4.45 V; (b) TEM image of C-LMO after first charge with SOC of 4.45 V; (c) SEM image of C-LMO after 96 h chemical delithiation; (d) TEM image of C-LMO after 96 h of chemical delithiation in $NO_2BF_4$.

charge. Meanwhile, transmission electron microscopy (TEM) in Figure 4b corroborates particle fracture through electrochemical shock during the first $Li^+$ extraction. To reproduce the electrochemical delithiation, we carried out chemical delithiation using the strong oxidant $NO_2^+$ to mimic the first charging process. Panels c and d in Figure 4 show the SEM and TEM images of the delithiated C-LMO after its reaction with $NO_2BF_4$ for 96 h. A large frequency of cracks occurs over the samples, similar to what is observed in the electrochemically charged C-LMO.

We have shown that particle fracture occurs during the first delithiation process, similar to what has been observed in $LiCoO_2$ cathode material during the first charge by an acoustic study.[14] Meanwhile, in the study of charge and discharge behaviors of Li/$MnO_2$ cells, Ohzuku also noticed microfractures by monitoring acoustic counts during the first electrochemical cycle.[15] Sastry and coworkers have also shown possible $LiMn_2O_4$ fractures in a combined AFM and simulation study.[37] We next studied X-ray diffraction to look for the structural changes associated with cracking. Figure 5

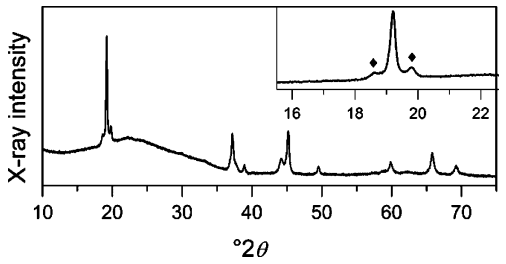


**Figure 5.** Powder X-ray diffraction pattern of C-LMO after first charge with SOC of 4.45 V. Newly evolved peaks are highlighted by the black diamonds.

shows the XRD pattern of C-LMO cathode at SOC of 4.45 V. The original (111) Bragg reflection at 18.8° splits into three new peaks: one major peak at 19.2° and two small peaks at 18.6 and 19.8°, which are highlighted in the inset. Those peaks can still be indexed to represent the (1 1 1) Miller plane. It is known that the cubic unit cell contracts during delithiation, which leads to the higher angle (right) shifts in the peaks that emerge at 19.2 and 19.8°. However, the peak at 18.6° hints a small lattice parameter expansion instead. This expansion has been observed by Aurbach in previous work.[38] We surmise that expansion occurs because of possible manganese migration into adjacent lithium tetrahedral sites during the electrochemical oxidation. Nevertheless, multiple phases were identified after the first charge, which could lead to the accumulation of strain in the active material that ultimately results in particle fracture.[39] Figure 6 shows the powder neutron diffraction (PND) pattern before and after the first charge. There is a drastic decrease in the diffraction intensity after lithium extraction, demonstrating the loss of long-range crystalline order. The diffraction pattern of the C-LMO with a SOC of 4.45 V is blown up in the inset for a detailed comparison. Peak splitting and broadening are observed after the first charge. The SOC potential of 4.45 V is above the delithiation two phase region as shown in the charging profiles. A single phase was expected at cell potential of ∼4.45 V. However, the lack of crystallinity after delithiation hinders precise indexing of solid phases.

We have shown in Figure 3 that the electrolyte and temperature-induced surface side reactions do not play significant role in influencing the irreversible capacity loss during the first cycle. Figure 7 shows that the first 100 cycles of the C-LMO in different solvent systems are unchanged; they too fade at a similar rate. In Figure 8, the neutron diffraction pattern is plotted for C-LMO at SOC of 3.40 V after 100 cycles in a lab-prepared $LiPF_6$ electrolyte. This pattern also shows multiple phases. Furthermore, the similarity between the neutron diffraction patterns of the firstly charged C-LMO

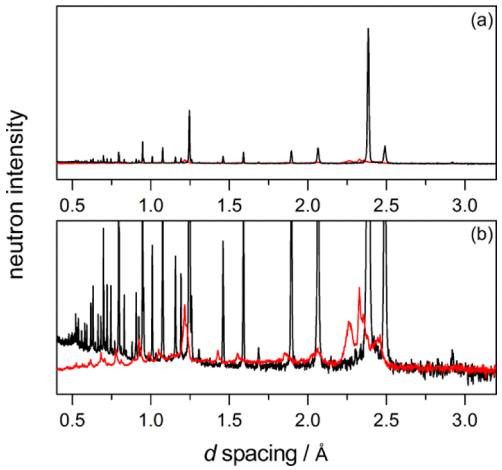


**Figure 6.** (a) PND pattern of fresh C-LMO (black) and the sample after first charge with SOC of 4.45 V (red); (b) close-up of the region near the baseline to show that new Bragg reflections emerge.

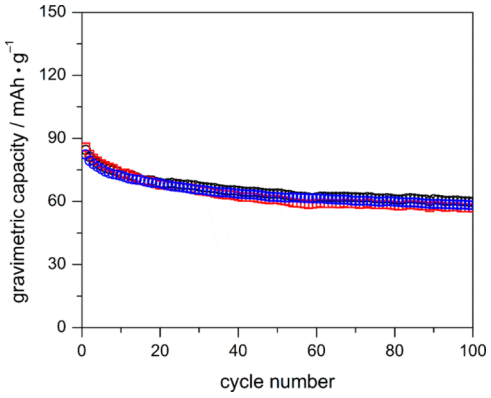


**Figure 7.** Comparison of the first 100 cycles of C-LMO in different solvents at room temperature: black circles, 1 M $LiAsF_6$ in EC:DEC mixture with v/v of 2:1; red squares, 1 M $LiPF_6$ in EC:DEC mixture with v/v of 2:1; blue triangles, 1 M $LiPF_6$ in DMC:EC:DEC with v/v/v of 1:1:1.

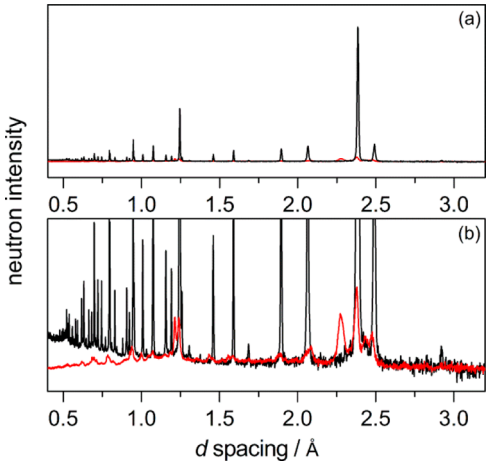


**Figure 8.** (a) PND pattern of fresh C-LMO (black) and the sample after 100 electrochemical cycles in 1 M $LiPF_6$ within EC:DEC mixture with v/v of 2:1 with SOC of 3.40 V (red); (b) close-up of the region near the baseline.

with SOC of 4.45 V and the pattern collected after 100 cycles with SOC of 3.40 V demonstrates that the loss of crystallinity upon the first charge is irreversible. This results matches that observed in Woodford's study on $LiCoO_2$ cathodes.[14]

Longer-term cycling of C-LMO is presented in Figure 9, showing ~43% capacity fade of the lithium manganese oxide

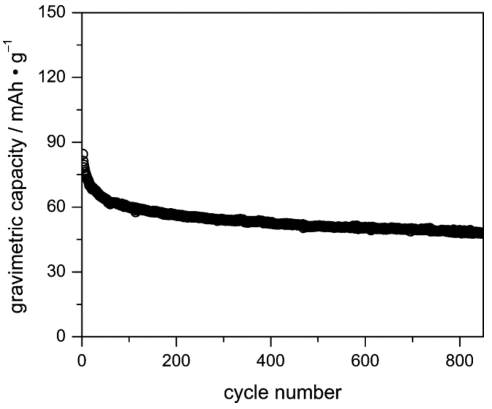


**Figure 9.** Cyclability of C-LMO over 850 cycles at 0.2 *C* current in 1 M $LiPF_6$ in 2:1 v/v EC:DEC at room temperature.

cathode over 850 cycles at 0.2 *C* current. The largest drop in capacity occurs over the roughly first 200 cycles, followed by more gradual capacity fade over the next ~650 cycles. The charge/discharge profiles of the 1st, 200th, and 800th cycle are plotted in Figure 10a. As we observed in the first cycle, there exist two distinct features corresponding to a single-phase and two-phase regions,[40] which can also be observed in the d*Q*/d*V* profile of Figure 10b from 3.9 to 4.2 V. The sharp features

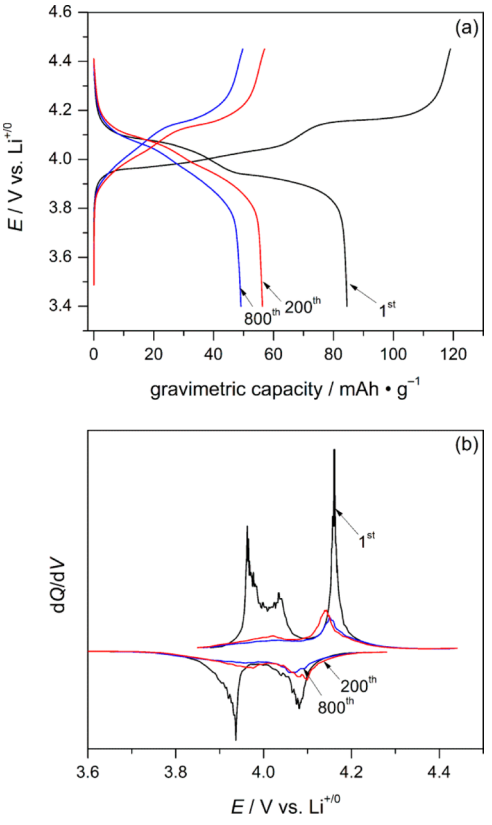


**Figure 10.** (a) Charge/discharge profiles of C-LMO at 1st, 200th, and 800th cycles obtained at 0.2 *C* current; (b) corresponding d*Q*/d*V* curves of 1st, 200th, and 800th cycles.


dx.doi.org/10.1021/am500671e | *ACS Appl. Mater. Interfaces* 2014, 6, 10849−10857

observed for the first cycle are smoothed in the 200th and 800th cycling data. In addition, there is a significant drop in peak intensity. Although there is still capacity fade observed from the 200th cycle to the 800th cycle in Figure 10a, their d$Q$/d$V$ curves nearly overlap, and the electrochemical features do not change significantly over the remaining 600 cycles. The phenomenon described above corroborates the crystallinity loss observed in the diffraction study. The reduced crystalline domain size suggests indistinguishable phase change boundaries, which is supported by diminished d$Q$/d$V$ peak intensities.[41] There have been similar discussions regarding the electrochemical behaviors $TiO_2$, $LiCoO_2$ and $LiNi_{0.5}Mn_{1.5}O_4$ with different crystalline sizes.[42−44]

Microstructural analysis after long-term cycling is presented in Figure 11. SEM imaging reveals that micrometer-sized active

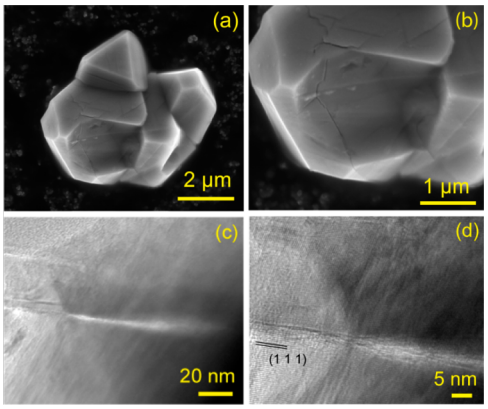


**Figure 11.** (a) SEM image of C-LMO after 850 electrochemical cycles; (b) enlarged SEM image showing cracks; (c) TEM image of C-LMO after 850 electrochemicals; (d) enlarged area showing the (111) family of planes.

material with clearly defined crystal facets is maintained after 850 cycles. Several particles aggregate during cycling, and we initially suspected that fracture would occur at those interfaces between aggregated particles due to the higher surface energy at boundaries. However, we observe that cracks are well-distributed all over surfaces as shown in panels a and b in Figure 11, which was not observed after the first cycle. This behavior hints that structural failure is more pronounced after prolonged electrochemical cycling; more microfractures are generated by repeated delithiation and lithiation. Figure 11c shows the typical TEM image of the cathode after long-term cycling with microscaled fracture identified. With higher magnification in Figure 11d, we see that fracture occurs along the (1 1 1) planes. In addtion, the twisted fringes suggest significant internal stress that results in structural collapse on the microscale.

## DISCUSSION

Capacity fade in $LiMn_2O_4$ is closely related to mechanical grinding, illustrated in Scheme 1. In a freshly prepared $LiMn_2O_4$ electrode, the bulk particles of active material are surrounded by the conductive carbon black network to enhance the electronic conductivity. Charge transfer occurs by lithium diffusion within an LMO particle, electron transfer at the LMO/carbon black interface, and also at LMO grain boundaries. However, after numerous charge/discharge cycles, fractures within active material propagate to increase the

**Scheme 1. Structural Changes and Interparticle Shearing of C-LMO Cathode Material during Electrochemical Cycling: Freshly Prepared Electrode (left); Electrode after Micro-Fracturing Occurs (right)**

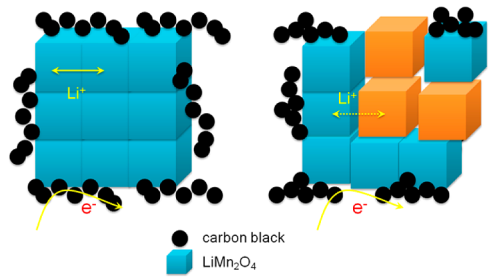


number of LMO/electrolyte interfaces. The smaller domains of the ruptured particles are electronically isolated due to the lack of contact with conductive additives or other LMO grains. Then, less access to the active cathode material leads to capacity loss as we observed. Meanwhile, it is noteworthy that this fracture does not stop after one electrochemical cycle. Rather, structural collapse occurs with continuous lithium insertion/extraction. Interestingly, from the long-term cyclability study, the majority of the capacity fade occurs during the first 200 cycles, and the true active cathode is a best described as a multiphase mixture of nanoscale domains.

The isolated domains should lead to an increase in the battery's internal resistance. Figure 12 shows the electro-

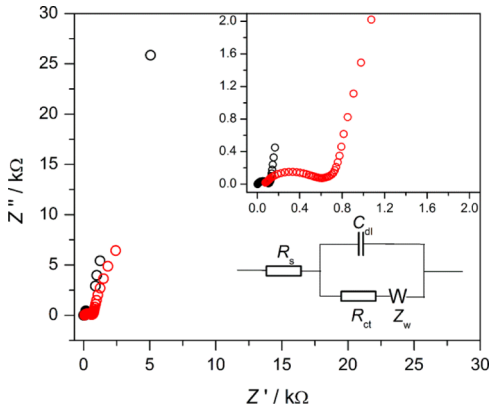


**Figure 12.** Electrochemical impedance spectra of a freshly prepared C-LMO half cell (black) and the cell after 850 electrochemical cycles with SOC of 3.40 V (red). The equivalent circuit is included in the plot.

chemical impedance spectrum of C-LMO half cells both before and after long-term cycling (850 cycles). A modified Randle's circuit was applied to describe the profiles. $R_s$ represents the solution resistance which matches the intersection at $Z'$ axis. The diameter of the semi-circle gives the charge transfer resistance as $R_{ct}$. In comparison with the freshly prepared cell, there is a large increase in both $R_s$ and $R_{ct}$ values which is consistent with Scheme 1.

The composition of C-LMO in this study shows an oxygen deficient structure that has been confirmed by elemental analysis and the neutron structural refinements. In our previous work, we have shown the electrochemical instability of oxygen-deficient $LiMn_2O_4$ compared to the stoichiometric spinel.[31] Therefore, to bridge the cathode's composition and structural properties with the failure mechanism we found, we introduced

two lab synthesized $LiMn_2O_4$ compounds with a controlled structure and oxygen level. On the basis of the elemental analysis, the two compounds are represented by the formulas $LiMn_2O_{4.03}$ and $LiMn_2O_{3.87}$, with manganese oxidation states of +3.53 and +3.37, respectively. We use these samples as representative examples of oxygen-stoichiometric (S-LMO) and oxygen-deficient (D-LMO) materials, respectively. The number of oxygen vacancies was selected to match that found in C-LMO; details of the characterization are presented in the Supporting Information. We recognize that crystal plane/surface morphology of the cathode materials could also contribute to the electrochemical performance of the battery,[45−47] but note that we control for these effects by synthesizing these compounds using the same solid-state method. Consequently, similar morphologies are expected, as illustrated in the SEM images as Figure S2 in the Supporting Information. Because of the oxygen vacancies in D-LMO, its lattice parameter of 8.253 Å is larger compared to 8.233 Å in S-LMO.

To validate the comparison, we cycled both of the materials under the same electrochemical conditions in lab-prepared $LiPF_6$ electrolyte as the C-LMO. The cyclability is plotted in Figure 13. Half cells prepared from both synthesized

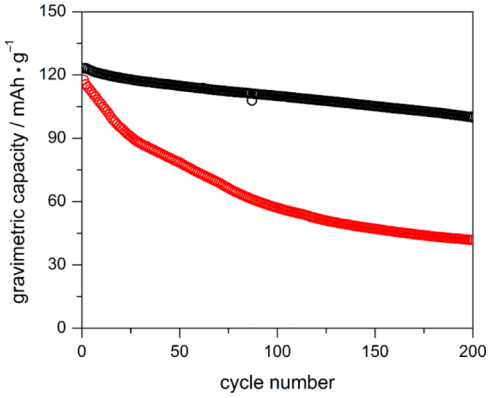


**Figure 13.** First 200 electrochemical cycles of S-LMO (black) and D-LMO (red) at 0.2 *C* current within the potential window of 3.40−4.45 V.

compounds show a similar initial discharge capacity of ∼120 mAh/g. However, there is a faster rate of capacity fade observed for the D-LMO. Over the first 200 cycles, the capacity of the S-LMO sample decreases to 98 mAh/g (81.6 % capacity retention), whereas, D-LMO decreases to only 64.2% of its initial capacity. We cycled the D-LMO for a longer period to achieve a better comparison with C-LMO, as shown in Figure S3 in the Supporting Information. Although the D-LMO sample is able to deliver higher capacity during the initial discharge, it shows a similar trend in capacity fade as that of C-LMO. Again, capacity fade occurs most markedly over the first 200 cycles, followed by relatively stable capacity retention over hundreds of cycles. Such a phenomenon indicates that the oxygen-deficient D-LMO sample might suffer a similar capacity fading mechanism as discussed earlier. An EIS study was performed on S-LMO and D-LMO cells after 100 cycles at 1*C* current. The data presented in Figure S8 in the Supporting Information show a significantly larger charge-transfer resistance for D-LMO after cycling, compared to S-LMO, which supports the deleterious effect of oxygen vacancies.

To confirm the capacity retention trend related to the oxygen content in LMO, we studied the microstructural properties of the lab prepared $LiMn_2O_4$ after 200 cycles as shown in Figure 14. Figure 14a shows that particles are largely intact, without

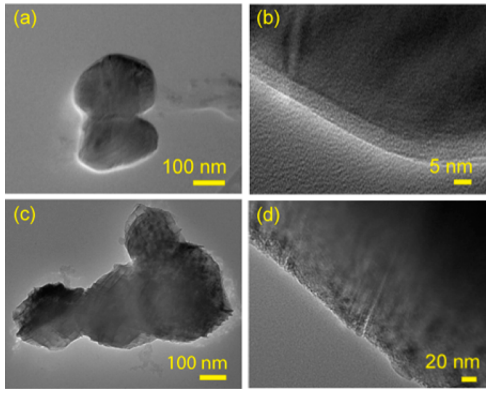


**Figure 14.** TEM images of lab prepared LMO after 200 cycles: (a, b) S-LMO; (c, d) D-LMO.

noticeable microfractures, which leads to better cyclability and structural stability. The enlarged image in Figure 14b conveys the same information. On the other hand, Figure 14c shows fractures and grain dislocations in cycled D-LMO. Microfractures can be identified at higher resolution Figure 14d. The results link the microstructure, capacity fade, and oxygen nonstoichiometry in $LiMn_2O_4$. These defects are detrimental to long-term capacity retention and structural integrity of spinel electrodes.

In Figure 15, we plot the XRD patterns of both lab-prepared LMO samples and their structural profiles after charging to 4.45 V SOC. Neither material shows the appearance of new phases although the peaks shift based on predicted lattice parameter changes. Moreover, slight peak broadening was observed for the both samples after the first charge. On the basis of the Rietveld refinement results, the crystalline domain size shrinks from 102.4 to 51.9 nm for S-LMO and 85.5 to 36 nm for D-LMO after the first electrochemical delithiation. All the structural patterns and refinement results are collected in Figures S4−S7 and Tables S5−S12 in the Supporting Information, from which we can calculate the lattice displacement based on isotropic volume change assumption. The lithium extraction from S-LMO results in a 0.161 Å lattice shrinkage; in the contrast, a 0.203 Å decrease in lattice parameter results from the oxygen-deficient sample. The 25% larger lattice expansion could result in more strain, which accounts for the difference in capacity retention.

## CONCLUSION

We have observed long-term capacity fade in commercially available $LiMn_2O_4$, which is shown to be oxygen-deficient. Powder diffraction and microstructural analysis have been carefully employed to observe account for structural failure. Surface side reactions and temperature do not play a significant role toward influencing the capacity retention. In contrast, we have shown that capacity fade arises due to structural collapse along the (1 1 1) planes. These microcracks lead to mechanical pulverization during electrochemical cycling of the cathodes, and leads to increased charge-transfer resistance within the cell.

This capacity fading mechanism is dependent on chemical composition. Similar fracture phenomena were illustrated in

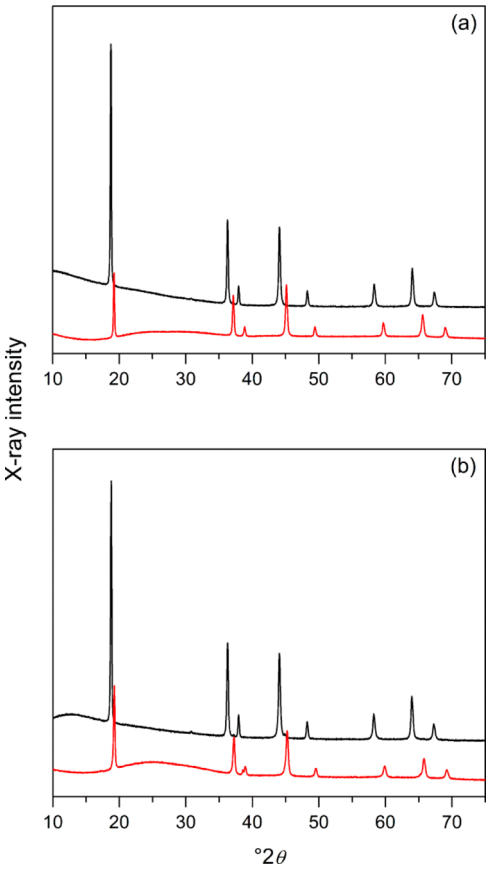


**Figure 15.** PXRD patterns of (a) as-prepared S-LMO (black) and its first charge delithiated sample (red) at SOC of 4.45 V; (b) as-prepared D-LMO (black) and its first charge delithiated sample (red) at SOC of 4.45 V.

lab-prepared oxygen-deficient LMO. However, near stoichiometric oxygen content gives rise to prolonged structural integrity and stable electrochemical cycling. Lattice strain is suggested to be one of the main reasons causing structural failures because of large volume changes. Current efforts focus on possible cation mixing during electrochemical cycling.

## ■ ASSOCIATED CONTENT

### Supporting Information

XRD and PND refinement parameters, elemental analyses, SEM images of synthesized samples, and EIS data for synthesized samples. This material is available free of charge via the Internet at http://pubs.acs.org./

## ■ AUTHOR INFORMATION

### Corresponding Author

*E-mail: bartmb@umich.edu. Tel: +1 (734) 615-9279.

### Notes

The authors declare no competing financial interest.

## ■ ACKNOWLEDGMENTS

This work was supported by in part by funding from the National Science Foundation (DMR-1253347) and in part by the General Motors/University of Michigan Advanced Battery Coalition for Drivetrains. We gratefully acknowledge Dr. Ashfia Huq at Oak Ridge National Laboratory Spallation Neutron Source POWGEN for experimental assistance with the neutron diffraction work. SEM and TEM characterization techniques at the University of Michigan Electron Microbeam Analysis Laboratory were funded by NSF grants DMR-0320710 and DMR-0315633, respectively.

## ■ REFERENCES

(1) Tarascon, J.−M.; Armand, M. Issues and Challenges Facing Rechargeable Lithium Batteries. *Nature* **2001**, *414*, 359−367.

(2) Mizushima, K.; Jones, P. C.; Wiseman, P. J.; Goodenough, J. B. $Li_xCoO_2$ ($0<x\leq1$): A New Cathode Material for Batteries of High Energy Density. *Mater. Res. Bull.* **1980**, *15*, 783−789.

(3) Ohzuku, T.; Ueda, A.; Nagayama, M. Electrochemistry and Structural Chemistry of $LiNiO_2$ (R 3m) for 4 volt Secondary Lithium Cells. *J. Electrochem. Soc.* **1993**, *140*, 1862−1870.

(4) Padhi, A. K.; Nanjundaswamy, K. S.; Goodenough, J. B. Phospho-Olivines as Positive-Electrode Materials for Rechargeable Lithium Batteries. *J. Electrochem. Soc.* **1997**, *144*, 1188−1194.

(5) Hunter, J. C. Preparation of a New Crystal Form of Manganese Dioxide: $\lambda$-$MnO_2$. *J. Solid State Chem.* **1981**, *39*, 142−147.

(6) Zhong, Q.; Bonakdarpour, A.; Zhang, M.; Gao, Y.; Dahn, J. R. Synthesis and Electrochemistry of $LiNi_xMn_{2-x}O_4$. *J. Electrochem. Soc.* **1997**, *144*, 205−213.

(7) Yazami, R. Touzain, Ph. A Reversible Graphite-Lithium Negative Electrode for Electrochemical Generators. *J. Power Sources* **1983**, *9*, 365−371.

(8) Yoshio, M.; Brodd, R. J.; Kozawa, A.; *Lithium-ion Batteries: Science and Technologies*; Springer: New York, 2010.

(9) Amatucci, G. G.; Tarascon, J. M.; Klein, L. C. Cobalt Dissolution in $LiCoO_2$-based Non-Aqueous Rechargeable Batteries. *Solid State Ionics* **1996**, *83*, 167−173.

(10) Huang, K.; Feng, M.; Goodenough, J.; Schmerling, M. Characterization of Sr-Doped $LaMnO_3$ and $LaCoO_3$ as Cathode Materials for a Doped $LaGaO_3$ Ceramic Fuel Cell. *J. Electrochem. Soc.* **1996**, *143*, 3630−3636.

(11) Wang, H.; Jang, Y.-I.; Huang, B.; Sadoway, D. R.; Chiang, Y.-M. Electron Microscopic Characterization of Electrochemically Cycled $LiCoO_2$ and $Li(Al,Co)O_2$ Battery Cathodes. *J. Power Sources* **1999**, *81−82*, 594−598.

(12) Wang, H.; Jang, Y.-I.; Huang, B.; Sadoway, D. R.; Chiang, Y.-M. TEM Study of Electrochemical Cycling-Induced Damage and Disorder in $LiCoO_2$ Cathodes for Rechargeable Lithium Batteries. *J. Electrochem. Soc.* **1999**, *146*, 473−480.

(13) Wang, D.; Wu, X.; Wang, Z.; Chen, L. Cracking Causing Cyclic Instability of $LiFePO_4$ Cathode Material. *J. Power Sources* **2005**, *140*, 125−128.

(14) Dokko, K.; Nishizawa, M.; Horikoshi, S.; Itoh, T.; Mohamedi, M.; Uchida, I. In situ Observation of $LiNiO_2$ Single-Particle Fracture during Li-Ion Extraction and Insertion. *Electrochem. Solid-State Lett.* **2000**, *3*, 125−127.

(15) Woodford, W. H.; Carter, W. C.; Chiang, Y.-M. Design Criteria for Electrochemical Shock Resistant Battery Electrodes. *Energy Environ. Sci.* **2012**, *5*, 8014−802.

(16) Ohzuku, T.; Tomura, H.; Sawai, K. Monitoring of Particle Fracture by Acoustic Emission during Charge and Discharge of Li/$MnO_2$ Cells. *J. Electrochem. Soc.* **1997**, *144*, 3496−3500.

(17) Wilson, J. R.; Cronin, J. S.; Barnett, S. A.; Harris, S. J. Measurement of Three-Dimensional Microstructure in a $LiCoO_2$ Positive Electrode. *J. Power Sources* **2011**, *196*, 3443−3447.

(18) Chen-Wiegart, Y.; Chen, K.; Liu, Z.; Faber, K. T.; Barnett, S. A.; Wang, J. 3D Analysis of a $LiCoO_2$−$Li(Ni_{1/3}Mn_{1/3}Co_{1/3})O_2$ Li-Ion Battery Positive Electrode using X-ray Nano-Tomography. *Electrochem. Comm.* **2013**, *28*, 127−130.

(19) Prada, E.; Di Domenico, D.; Creff, Y.; Bernard, J.; Sauvant-Moynot, V.; Huet, F. A Simplified Electrochemical and Thermal Aging Model of $LiFePO_4$-Graphite Li-Ion Batteries: Power and Capacity Fade Simulations. *J. Electrochem. Soc.* **2013**, *160*, A616−A628.

(20) Lee, S.; Oshima, Y.; Hosono, E.; Zhou, H.; Kim, K.; Chang, H. M.; Kanno, R.; Takayanagi, K.; In-situ, TEM Observation of Local

Phase Transformation in a Rechargeable $LiMn_2O_4$ Nanowire Battery. *J. Phys. Chem. C* **2013**, *117*, 24236−24241.
(21) Ma, Z.; Li, T.; Huang, Y. L.; Liu, J.; Zhou, Y.; Xue, D. Critical Silicon-Anode Size for Averting Lithiation-Induced Mechanical Failure of Lithium-Ion Batteries. *RSC Adv.* **2013**, *3*, 7398−7402.
(22) Pharr, M.; Suo, Z.; Vlassak, J. J. Measurements of the Fracture Energy of Lithiated Silicon Electrodes of Li-Ion Batteries. *Nano Lett.* **2013**, *13*, 5570−5577.
(23) Liang, W.; Hong, L.; Yang, H.; Fan, F.; Liu, Y.; Li, H.; Li, J.; Huang, J. Y.; Chen, L.-Q.; Zhu, T.; Zhang, S. Nanovoid Formation and Annihilation in Gallium Nanodroplets under Lithiation-Delithiation Cycling. *Nano Lett.* **2013**, *13*, 5212−5217.
(24) McDowell, M. T.; Lee, S. W.; Nix, W. D.; Cui, Y. 25th Anniversary Article: Understanding the Lithiation of Silicon and Other Alloying Anodes for Lithium-Ion Batteries. *Adv. Mater.* **2013**, *25*, 4966−4984.
(25) Liu, X. H.; Zhong, L.; Huang, S.; Mao, S. X.; Zhu, T.; Huang, J. Y. Size-Dependent Fracture of Silicon Nanoparticles during Lithiation. *ACS Nano* **2012**, *6*, 1522−1531.
(26) Bhattacharya, S.; Riahi, A. R.; Alpas, A. T. A Transmission Electron Microscopy Study of Crack Formation and Propagation in Electrochemically Cycled Graphite Electrode in Lithium-Ion Cells. *J. Power Sources* **2011**, *196*, 8719−8727.
(27) Qi, Y.; Xu, Q.; Van der Ven, A. Chemically Induced Crack Instability When Electrodes Fracture. *J. Electrochem. Soc.* **2012**, *159*, A1838−A1843.
(28) Christensen, J.; Newman, J. A Mathematical Model of Stress Generation and Fracture in Lithium Manganese Oxide. *J. Electrochem. Soc.* **2006**, *153*, A1019−A1030.
(29) Aifantis, K. E.; Dempsey, J. P. Stable Crack Growth in Nanostructured Li-Batteries. *J. Power Sources* **2005**, *143*, 203−211.
(30) Zhu, M.; Park, J.; Sastry, A. M. Fracture Analysis of the Cathode in Li-Ion Batteries: A Simulation Study. *J. Electrochem. Soc.* **2012**, *159*, A492−A498.
(31) Hao, X.; Gourdon, O.; Liddle, B. J.; Bartlett, B. M. Improved Electrode Kinetics in Lithium Manganospinel Nanoparticles Synthesized by Hydrothermal Methods: Identifying and Eliminating Oxygen Vacancies. *J. Mater. Chem.* **2012**, *22*, 1578−1591.
(32) Yonemura, M.; Yamada, A.; Kobayashi, H.; Tabuchi, M.; Kamiyama, T.; Kawamoto, Y.; Kanno, R. Synthesis, Structure, and Phase Relationship in Lithium Manganese Oxide Spinel. *J. Mater. Chem.* **2004**, *14*, 1948−1958.
(33) Palacin, M. R.; Chabre, Y.; Dupont, L.; Hervieu, M.; Strobel, P.; Rousse, G.; Masquelier, C.; Anne, M.; Amatucci, G. G.; Tarascon, J. M. On the origin of the 3.3 and 4.5 V Steps Observed in $LiMn_2O_4$-Based Spinels. *J. Electrochem. Soc.* **2000**, *147*, 845−853.
(34) Yamada, A.; Tanaka, M. Jahn-Teller Structural Phase Transition Around 280K in $LiMn_2O_4$. *Mater. Res. Bull.* **1995**, *30*, 715−721.
(35) Oikawa, K.; Kamiyama, T.; Izumi, F.; Chakoumakos, B. C.; Ikuta, H.; Wakihara, M.; Li, J.; Matsui, Y. Structural Phase Transition of the Spinel-Type Oxide $LiMn_2O_4$. *Solid State Ionics* **1998**, *109*, 35−41.
(36) Xu, K. Nonaqueous Liquid Electrolytes for Lithium-Based Rechargeable Batteries. *Chem. Rev.* **2004**, *104*, 4303−4417.
(37) Hun, J.; Chung, M.; Park, M.; Woo, S.; Zhang, X.; Sastry, A. M. Generation of Realistic Particle Structures and Simulations of Internal Stress: A Numerical/AFM Study of $LiMn_2O_4$ Particles. *J. Electrochem. Soc.* **2011**, *158*, A434−A439.
(38) Aurbach, D.; Levi, M. D.; Levi, E.; Markovsky, B.; Salitra, G.; Teller, H.; Heider, U.; Heider, L. On the Electroanalytical Characterization of $Li_xCoO_2$, $Li_xNiO_2$ and $LiMn_2O_4$ (Spinel) Electrodes in Repeated Lithium Intercalation-Deintercalation Processes. *MRS Proc.* **1998**, *496*, 435−441.
(39) Thurston, T. R.; Jisrawi, N. M.; Mukerjee, S.; Yang, X. Q.; McBreen, J.; Daroux, M. L.; Xing, X. K. Synchrotron X-ray Diffraction Studies of the Structural Properties of Electrode Materials in Operating Battery Cells. *Appl. Phys. Lett.* **1996**, *69*, 194−196.
(40) Mukerjee, S.; Thurston, T. R.; Jisrawi, N. M.; Yang, X. Q.; McBreen, J.; Daroux, M. L.; Xing, X. K. Structural Evolution of $Li_xMn_2O_4$ in Lithium Ion Battery Cells Measured in Situ using Synchrotron X-ray Diffracion Techniques. *J. Electrochem. Soc.* **1998**, *145*, 466−472.
(41) Kim, J. H.; Yoon, C. S.; Myung, S. T.; Prakash, J.; Sun, Y. K. Phase Transitions in $Li_{1-\delta}Ni_{0.5}Mn_{1.5}O_4$ During Cycling at 5 V. *Electrochem. Solid-State Lett.* **2004**, *7*, A216−A220.
(42) Wagemaker, M.; Borghols, W. J. H.; Mulder, F. M. Large Impact of Particle Size on Insertion Reactions. A Case for Anatase $Li_xTiO_2$. *J. Am. Chem. Soc.* **2007**, *129* (14), 4323−4327.
(43) Jo, M.; Hong, Y.-S.; Choo, J.; Cho, J. Effect of $LiCoO_2$ Cathode Nanoparticle Size on High Rate Performance for Li-Ion Batteries. *J. Electrochem. Soc.* **2009**, *156*, A430−A434.
(44) Kovacheva, D.; Markovsky, B.; Salitra, G.; Talyosef, Y.; Gorova, M.; Levi, E.; Riboch, M.; Kim, H.-J.; Aurbach, D. Electrochemical Behavior of Electrodes Comprising Micro- and Nano-Sized Particles of $LiNi_{0.5}Mn_{1.5}O_4$: A Comparative Study. *Electrochim. Acta* **2005**, *50*, 5553−5560.
(45) Karim, A.; Fosse, S.; Persson, K. A. Surface Structure and Equilibrium Particle Shape of the $LiMn_2O_4$ Spinel from First Principles Calculations. *Phys. Rev. B* **2013**, *87*, 075322−075326.
(46) Kim, J. S.; Kim, K. S.; Cho, W. H.; Kanno, R.; Choi, J. W. A Truncated Manganese Spinel Cathode for Excellent Power and Lifetime in Lithium-Ion Batteries. *Nano Lett.* **2012**, *12*, 6358−6365.
(47) Chemelewski, K. R.; Lee, E. S.; Li, W.; Manthiram, A. Factors Influencing the Electro-chemical Properties of High Voltage Spinel Cathodes: Relative Impact of Morphology and Cation Ordering. *Chem. Mater.* **2013**, *25*, 2890−2897.